International Communications in Heat and Mass Transfer 118 (2020) 104877

Contents lists available at ScienceDirect

International Communications in Heat and Mass Transfer

journal homepage: www.elsevier.com/locate/ichmt

Computational investigation of annular flow condensation in microgravity with two-phase inlet conditions

Yue Qiu[a], Hyoungsoon Lee[b], Chirag R. Kharangate[a,*]

[a] Department of Mechanical and Aerospace Engineering, Case Western Reserve University, 10900 Euclid Avenue, Cleveland, OH 44106, USA
[b] School of Mechanical Engineering, Chung-Ang University, Seoul, South Korea

ARTICLE INFO

Keywords:
CFD
Condensation
Heat transfer
Interface
Phase-change

ABSTRACT

Condensation heat exchangers contribute significantly to the size of the thermal management system, and their implementation in future spacecraft will require a better understanding of the underlying heat transfer phenomena. In this study, we computationally investigate flow condensation in microgravity with two-phase inlet conditions utilizing the VOF multi-phase model and a 2-dimensional axisymmetric domain. The model is validated utilizing experiments from prior microgravity flow condensation tests conducted onboard a parabolic flight. A control-volume-based theoretical model is utilized to estimate the inlet vapor fraction and inlet phase velocity boundary conditions. The computational model predicts complex flow behavior occurring at the two-phase interface during condensation, but the model suffers from some liquid accumulation in the vapor region. Local condensation heat transfer is under-estimated in the inlet section, and over-estimated in the exit section, compared with the experimental measurements. Mean condensation heat transfer coefficients compare well to experiments. Results show a need for full 3D simulations of flow condensation to improve predictions of liquid entrainment and liquid deposition phenomena that significantly influence local heat transfer coefficients predictions

1. Introduction

1.1. Two-phase flows for space applications

NASA is planning future missions not only to send robotic landers as far as Europa but also land humans on Mars. To develop advanced aircraft capable of such long-duration missions, spacecraft thermal control technology needs to become more compact, have high efficiency, and have low weight and volume. Traditional thermal management systems have relied heavily on single-phase air and liquid cooling designs. However, these systems cannot meet the heat dissipation needs necessary for future long-term space missions. Therefore, engineers are now exploring better thermal management systems, including utilizing two-phase flows because of the higher heat transfer performance over single-phase flows [1]. This has led to unprecedented development in understanding heat acquisition components utilizing flow boiling as the cooling scheme. This includes work on mini/microchannel flows [2,3], jet and spray cooling [4–6]. While we have seen significant work in understanding heat acquisition in the last few decades, less importance has been given to heat rejection components like condensation heat exchangers that also contribute significantly to the size of the system.

1.2. Flow condensation prediction

Condensation is a two-phase phenomenon that involves phase-change from vapor to liquid. An efficient design of a condensation heat exchanger requires techniques that can accurately predict the flow pattern and corresponding thermal behavior during this phase-change process. Flow patterns and flow transitions depend on many factors including gravity, specific pressure, heat flux, flow rate, and channel geometry [7]. For example, horizontal tubes in Earth gravity show a variety of flow patterns including annular, annular-mist, semi-annular, slug, plug, wavy and stratified flow regimes [7]. A lot of research has been done to develop simple relations for flow transitions including the development of flow pattern maps [8–13], but this technique suffers from deficiencies since a universal map that is applicable to all flow and geometric configurations cannot be created.

With this deficiency in predicting flow transitions, researchers predict heat transfer in condensing flows using four common approaches. Empirical and semi-empirical correlations are the most common way condensation heat transfer is predicted by researchers

* Corresponding author.
E-mail address: chirag.kharangate@case.edu (C.R. Kharangate).

https://doi.org/10.1016/j.icheatmasstransfer.2020.104877

0735-1933/ © 2020 Elsevier Ltd. All rights reserved.

Nomenclature

A	area
$A_{f,*}$	cross-section area of liquid control volume
A^+	parameter in eddy diffusivity model
Δc	mesh size
c_p	specific heat at constant pressure
D	diameter
E	specific internal energy (J/kg)
f	friction factor
G	mass velocity (kg/m^{2}s)
h	local condensation heat transfer coefficient
h_{fg}	latent heat
I	turbulence intensity
K	Von-Karman constant
k	thermal conductivity
$\dot{m}$	mass flow rate
$\dot{m}''$	interfacial mass flux
M	molecular weight
P	pressure
P_f	perimeter
$P_{f,y}$	cross-section perimeter, $P_{f,y} = \pi(D_i - 2y)$
$P_{f,\delta}$	cross-section perimeter of the interface, $P_{f,\delta} = \pi(D_i - 2\delta)$
P_r	Prandtl number
$Pr_{f,T}$	turbulent Prandtl number
Q	energy source (W/m^3)
q	heat transfer rate
q"	heat flux
r_i	mass transfer intensity (s^{-1})
R	universal gas constant
Re	Reynolds number
S	mass source (kg/m^3s)
Δt	time period for averaging
T	temperature
u	axial velocity
u^*	friction velocity, $u^* = \sqrt{\tau_{wall}/\rho_f}$
W	mass flow rate
x	vapor quality
x_e	thermodynamic equilibrium quality
y	distance perpendicular to wall
$y+$	dimensionless distance perpendicular to wall, $y^+ = yu^*/\nu_f$
z	stream-wise coordinate

Greek symbols

α	volume fraction
γ	accommodation coefficient
Γ_{fg}	condensation mass transfer rate per unit axial distance
δ	liquid film thickness
δ^+	dimensionless liquid film thickness, $\delta^+ = \delta u^*/\nu_f$
ϵ_m	eddy momentum diffusivity
μ	dynamic viscosity
ν	kinematic viscosity
ρ	density
τ	shear stress

Superscripts

$-$	time average
$\rightarrow$	vector
'	fluctuation

Subscripts

c	condensation
e	evaporation
exp	experimental
eff	effective
f	saturated liquid
FC	FC-72
g	saturated vapor
h	hydraulic
i	interfacial, inner surface of condensation tube
in	inlet of condensation length
o	outer surface of condensation tube
sat	saturation
wall	wall
w	water
avg	spatial average

[14–23]. These correlations are developed by performing experiments over a specific range of parameters. It is advisable not to use them outside the parametric range due to the complex behavior observed in flow condensation systems. A more effective approach is generalized correlations that are developed by utilizing data from various worldwide experimental databases [24,25]. These have greater validity as they are generated utilizing a considerable number of data points and parametric ranges. Another approach is the use of mechanistic or theoretical model [26]. Theoretical models like the annular flow model [26] can predict steady-state variations of fluid flow and thermal behavior. However, their applicability is narrow and can only predict accurately for specific flow regimes. Recent progress in computing techniques has facilitated the development of computational fluid dynamics simulations (CFD) to predict phenomena like flow condensation. CFD models are very promising in comparison to traditional techniques because they can predict detailed transient variations in individual phase velocities, void fractions and corresponding temperatures, not possible with other techniques. An accurate CFD model can not only address the flow transitions but also the corresponding heat transfer behaviors.

1.3. CFD in condensation

The past decade has seen researchers performing numerous CFD investigations on flow condensation. *Da* Riva and Del Col [27] utilized the volume of fluid (VOF) method to investigate flow condensation in a microchannel with R134a as the working fluid. The model was able to capture, for different flows rates, the competing effects of gravity and inertia. Ganapathy et al. [28] also utilized the VOF method to investigate flow condensation in a microchannel with R134a as the working fluid. Flow pattern matched experimental behavior, and pressure drop and heat transfer predictions did well with prior correlations. Vyskocil et al. [29] performed CFD modeling for air-steam flow condensation. Experiments on a flat plate were performed, and the model was seen to be effective in predicting experimental condensation rates and vapor concentrations. Yin et al. [30] investigated condensation in a horizontal minitube by utilizing the VOF method and studied the effect of non-condensable gas with water as the working fluid. Results showed that the presence of non-condensable gases compromises the performance. Qiu et al. [31] investigated condensation in a spiral tube with propane as the working fluid. In their study, they also considered entrainment of liquid in the vapor modeling. The model could capture the flow pattern transitions between stratified, annular and mist flow. Heat transfer and pressure drops predictions agreed well with their experiments. Zhang et al. [32] utilized the VOF method to study flow condensation in a minichannel. Heat transfer and pressure drop predictions agreed well with correlations. Lee et al. [33] utilized the VOF method to investigate condensation in downward flow tube with FC-72 as the working fluid. The predicted heat transfer agreed well with experiments. Kharangate et al. [34] investigated upflow condensation in a tube utilizing the VOF method with FC-72 as the working fluid. They studied interfacial behavior, condensation heat transfer coefficients as well as local fluid temperature variation across the two-phase interface. Interfacial waviness, flooding and climbing film conditions were also captured in the void fraction contours. The predicted heat transfer agreed well with experiments. Zhang et al. [35] investigated condensation in a tube in horizontal orientation. Pressure drop and heat transfer predicted data fit well with several empirical/semi-empirical correlations from literature. Wen et al. [36] investigated condensation in horizontal flattened tubes. They investigated tube configurations with different shapes, aspect ratios, and inlet vapor qualities. Using their data, they developed improved correlations for flattened tubes. Deng et al. [37] utilized the VOF method to investigate upflow condensation in a flat tube with R134a as the working fluid.

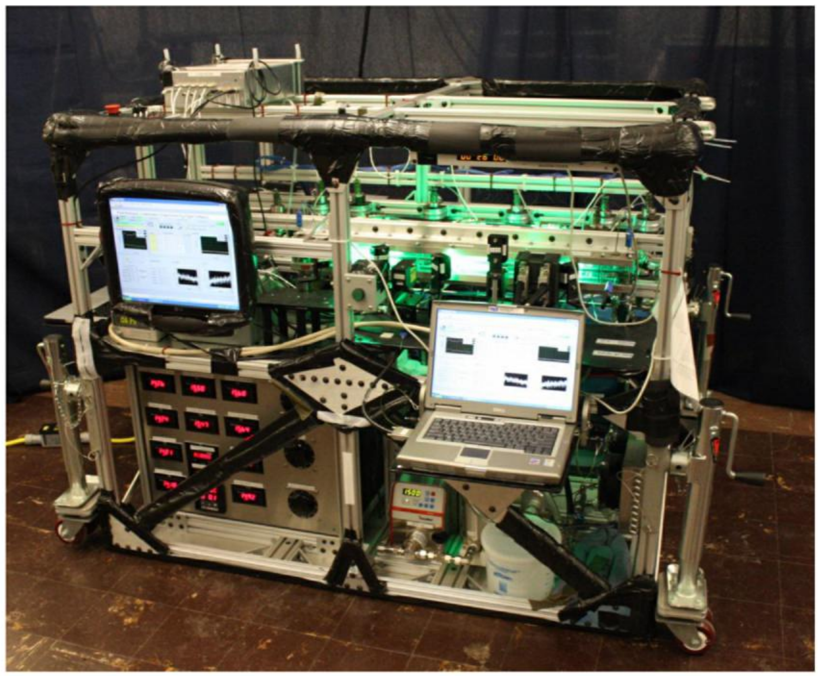

(a)

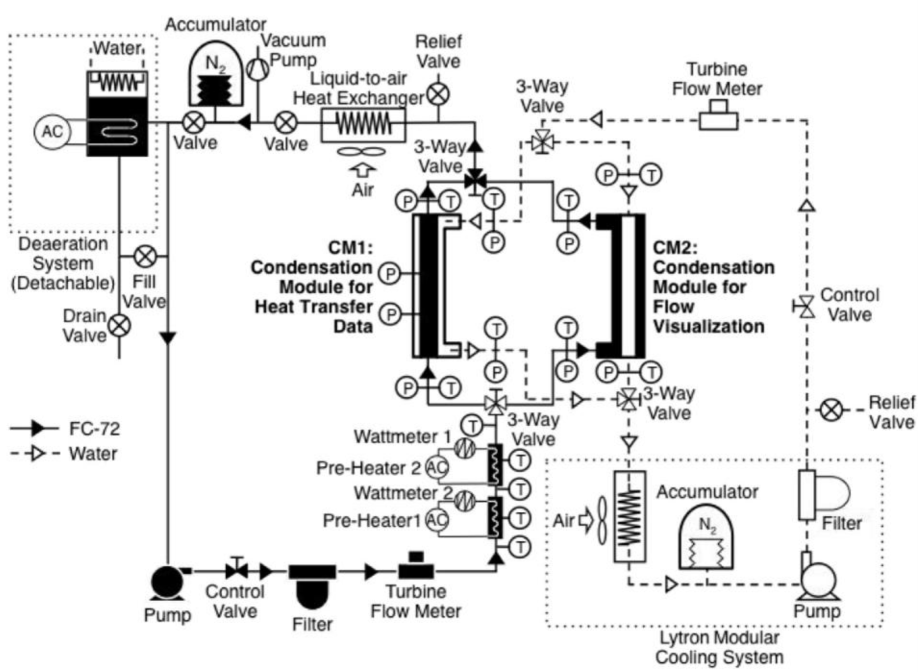

(b)

Fig. 1. (a) Flow boiling and condensation test rig. (Adapted from [41]) (b) Schematic of the two-phase flow conditioning loop. (Adapted from [40]).

Their model predicted complex interfacial behavior like waviness, entrainment, and calculated condensation parameters like thickness and interfacial shear stress. Zhao et al. [38] investigated flow condensation in a semicircular channel. Using their data, they developed improved correlations for pressure drop and heat transfer. Abadi et al. [39] investigated steam condensation along an inclined flat channel. Void fraction showed drop-wise condensation as the condensation mechanism. Heat transfer and pressure drop predictions agreed well with experiments and prior correlations.

1.4. Objectives

In this study, we investigate flow condensation in a circular tube under microgravity conditions with two-phase inlet conditions. While experimental data for turbulent condensing flow from prior research exists, no work to validate the condensation phenomena with computational model in similar configurations under microgravity has been done before. Two mass transfer models will be used to capture the phase-change process. The temperature variation in and around the two-phase interface will be investigated. The predictions of the computational model are validated using data from prior microgravity flow condensation tests conducted onboard a parabolic flight [40]. The experimental data for heat transfer coefficient and temperature will be compared with the predictions to understand model performance.

2. Experimental methods

2.1. Condensation facility

Experimental data obtained from Purdue University Boiling and Two-Phase Flow Laboratory (PU-BTPFL) flow boiling and flow condensation parabolic flight facility shown in Fig. 1(a) [41] will be utilized in the current study. The flow schematic is shown in Fig. 1(b) [40]. This facility includes 2 flow loops. The main flow loop is for FC-72 and the second flow loop is for cooling water. A gear pump is utilized to pump FC-72 through the primary flow loop. After the pump, the loop includes a control valve and a flow meter. Two inline pre-heaters are used to heat the fluid to the desired inlet thermodynamic quality test conditions before the fluid enters the condensation test section. After the condensation test section, the two-phase mixture is condensed using a water-to-liquid condenser. The secondary water flow loop is designed to accept heat in the test section from the FC-72. Another pump drives the water through the secondary flow loop, which then flows through a flow meter. The water is heated in the condensation module and is cooled by an air-cooled heat exchanger before being routed back to the pump.

The experimental facility consists of two test sections for condensation [40]. The first test section, CM-HT, is utilized to conduct heat transfer experiments. This test module has a tube-in-tube counter flow configuration with FC-72 on the inside, and water on the outside as shown in Fig. 2(a). The second test section, CM-FV, is utilized to conduct flow investigation of the condensing film with similar inlet flow conditions as the CM-HT. This test module also has an annular counter flow configuration, but with FC-72 on the outside, and water on the

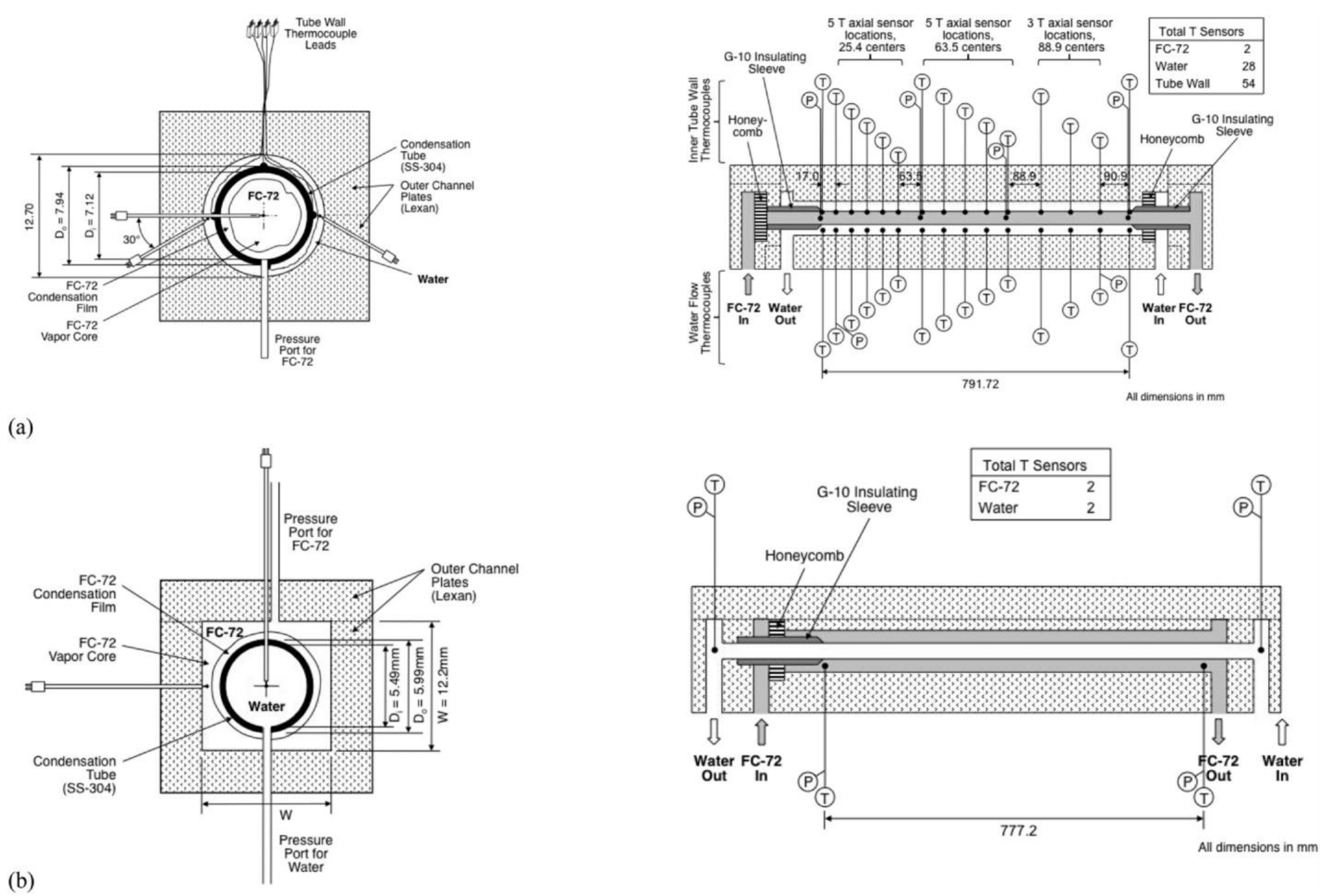

Fig. 2. Cross-sectional and longitudinal schematics of (a) the condensation module for heat transfer measurements, CM-HT, and (b) the condensation module for flow visualization, CM-FV. (Adapted from [40]).

Table 1
Test conditions for the CFD simulations.

	G[kg/m^{2}s]	G_w[kg/m^{2}s]	$x_{e,\ in}$	$x_{e,\ out}$	$P_{FC,\ in}$[Pa]	T_{sat}[K]
Case 1	128.99	220.92	0.89	0.14	121,104.6	335.56
Case 2	148.48	224.98	0.71	0.16	113,671.9	333.48
Case 3	177.79	278.56	0.89	0.25	121,104.6	335.41

inside as shown in Fig. 2(b). Important dimensions of the test modules have been shown in Fig. 2(a) and (b).

2.2. Operating conditions

From the database of experiments conducted in [40], for this study, three experimental test cases were made available from PU-BTPFL. These experiments were conducted in microgravity conditions onboard a parabolic flight. Table 1 shows the operating conditions including the FC-72 flow rates, water flow rates, inlet temperatures, pressures and thermodynamic qualities for these experimental test cases.

3. Computational model

3.1. Conservation equations

Conservation equations are computed by the VOF method in FLUENT [42]. The continuity equations for the two phases are given as:

$$\frac{\partial}{\partial t}(\alpha_f \rho_f) + \nabla\cdot(\alpha_f \rho_f \vec{u}_f) = S_f \tag{1a}$$

and

$$\frac{\partial}{\partial t}(\alpha_g \rho_g) + \nabla\cdot(\alpha_g \rho_g \vec{u}_g) = S_g \tag{1b}$$

where S_f and S_g are the volumetric source terms. The conservation equation for momentum is given as:

$$\frac{\partial}{\partial t}(\rho\vec{u}) + \nabla\cdot(\rho\vec{u}\,\vec{u}) = -\nabla P + \nabla\cdot[\mu(\nabla\vec{u} + \nabla\vec{u}^{T})] + \vec{F} \tag{2}$$

and the conservation equation for energy is given as:

$$\frac{\partial}{\partial t}(\rho E) + \nabla\cdot(\vec{u}(\rho E + P)) = \nabla\cdot(k_{eff}\nabla T) + Q \tag{3}$$

where Q is the energy source term given as follows:

$$Q = h_{fg} S_f \tag{4}$$

The continuum surface force model proposed by Brackbill et al. [43] is used in the momentum equation to model surface tension.

Turbulence is modeled utilizing the standard k − ω turbulence model with shear stress transport formulation [42]. A damping factor of 10 is utilized. This specific methodology was selected based on a thorough optimization conducted by Lee et al. [33] in their study on

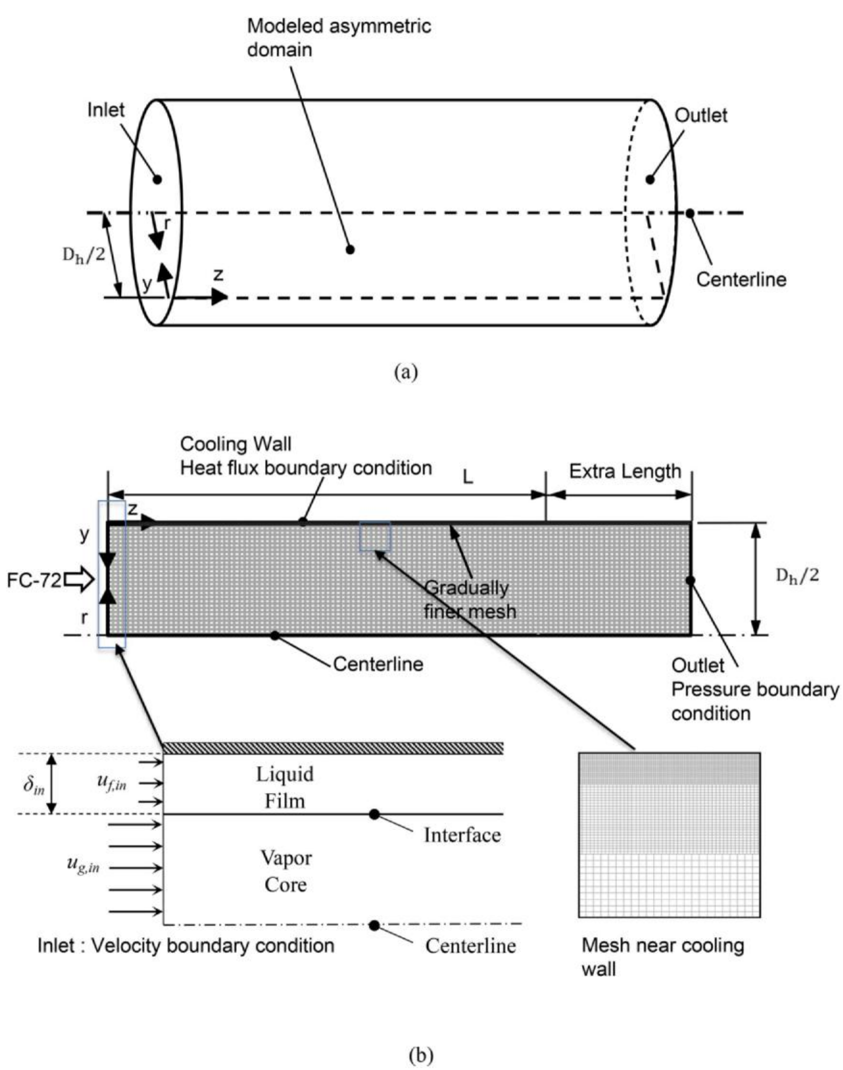

Fig. 3. (a) Cylindrical domain for the computational model. (b) 2-D axisymmetric domain with mesh modeled in the present study and boundary conditions.

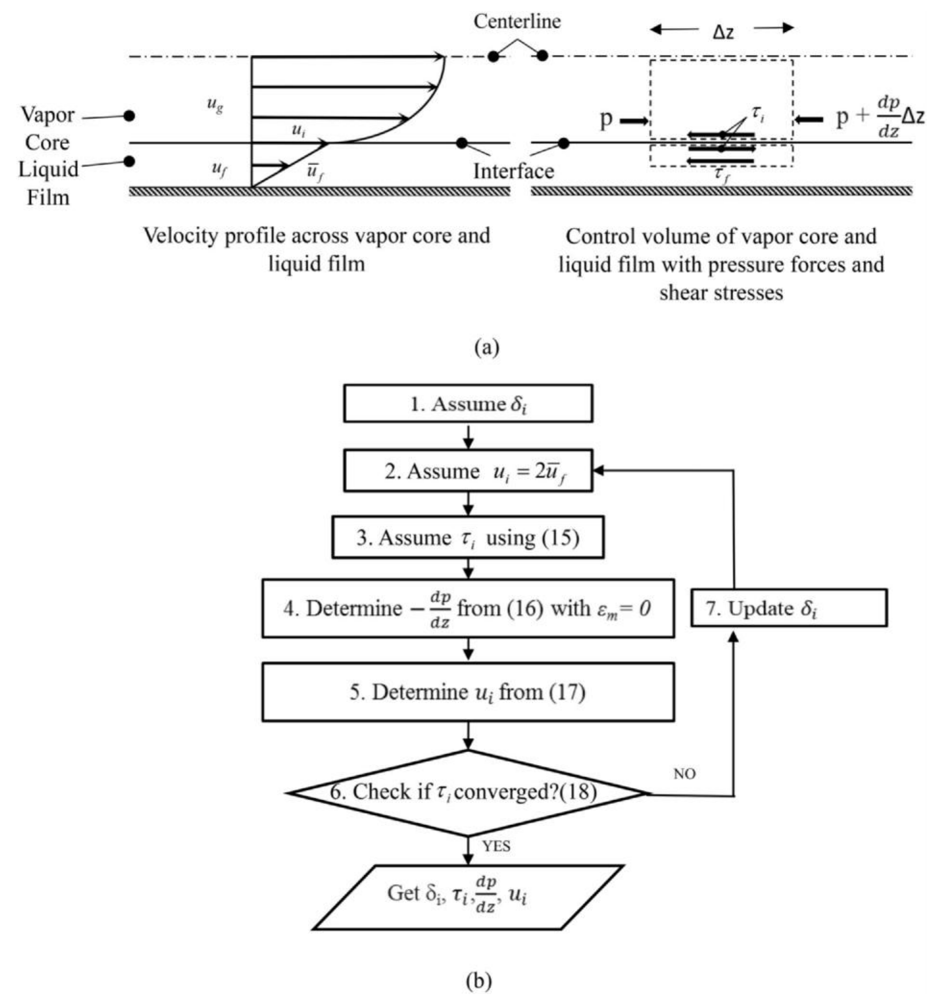

Fig. 4. (a) Velocity profile and control volume of vapor core and liquid film. (b) Flow chart for computing initial thickness. Adapted from [47].

Table 2
Summary of final equations based on the Annular flow model by [47].

Liquid shear stress	$\tau_f = \left(-\frac{dp}{dz}\right)\frac{A_{f,*}}{P_{f,y}} + \frac{\tau_i P_{f,\delta} + \Gamma_{fg} u_i}{P_{f,y}} = \mu_f\left(1 + \frac{\varepsilon_m}{\upsilon_f}\right)\frac{du_f}{dy}$ (12)
Interfacial sheer stress based on [50]	$\tau_i = \frac{1}{2} f_i \rho_g (\bar{u}_g - u_i)^2 + \frac{\Gamma_{fg}(\bar{u}_g - u_i)}{2P_{f,\delta}}$ (13)
Pressure drop	$-\frac{dp}{dz} = \dfrac{\frac{\mu_f \dot{m}_f}{\rho_f \delta^2}(\tau_i P_{f,\delta} + \Gamma_{fg} u_i)\int_0^1 \left[P_{f,y}\int_0^{y/\delta}\frac{1}{P_{f,y}}\left(1 + \frac{\varepsilon_m}{\upsilon_f}\right)^{-1} d\left(\frac{y}{\delta}\right)\right] d\left(\frac{y}{\delta}\right)}{\int_0^1 \left[P_{f,y}\int_0^{y/\delta}\frac{A_{f,*}}{P_{f,y}}\left(1 + \frac{\varepsilon_m}{\upsilon_f}\right)^{-1} d\left(\frac{y}{\delta}\right)\right] d\left(\frac{y}{\delta}\right)}$ (14)
Interfacial velocity	$u_i = \dfrac{\left(-\frac{dp}{dz}\right)\frac{\delta}{\mu_f}\int_0^1 \frac{A_{f,*}}{P_{f,y}}\left(1 + \frac{\varepsilon_m}{\upsilon_f}\right)^{-1} d\left(\frac{y}{\delta}\right) + \frac{\delta}{\mu_f}(\tau_i P_{f,\delta})\int_0^1 \frac{1}{P_{f,y}}\left(1 + \frac{\varepsilon_m}{\upsilon_f}\right)^{-1} d\left(\frac{y}{\delta}\right)}{1 - \frac{\delta}{\mu_f}\Gamma_{fg}\int_0^1 \frac{1}{P_{f,y}}\left(1 + \frac{\varepsilon_m}{\upsilon_f}\right)^{-1} d\left(\frac{y}{\delta}\right)}$ (15)
Interfacial shear stress	$\tau_i = \dfrac{-A_g \frac{dp}{dz} + \frac{d}{dz}(\rho_g \bar{u}_g^2 A_g) + \Gamma_{fg} u_i}{P_{f,\delta}}$ (16)
Eddy momentum diffusivity	$\frac{\varepsilon_m}{\upsilon_f} = -\frac{1}{2} + \frac{1}{2}\sqrt{1 + 4K^2 y^{+2}\left[1 - \exp\left(-\sqrt{\frac{\tau_f}{\tau_{wall}}}\frac{y^+}{A^+}\right)\right]^2 \frac{\tau}{\tau_{wall}}\left(1 - \frac{y^+}{\delta^+}\right)^{0.1}}$ (17)

downward flow condensation.

3.2. Mass transfer model

The mass transfer rate during flow condensation can be calculated utilizing a mass transfer model. Two kinds of mass transfer models have been used in many CFD investigations involving phase-change. The first one is the model by Lee [44]. An assumption of quasi thermo-equilibrium state is made in the model. The corresponding mass transfer is calculated based on the local deviation from T_{sat}, according to the following relations:

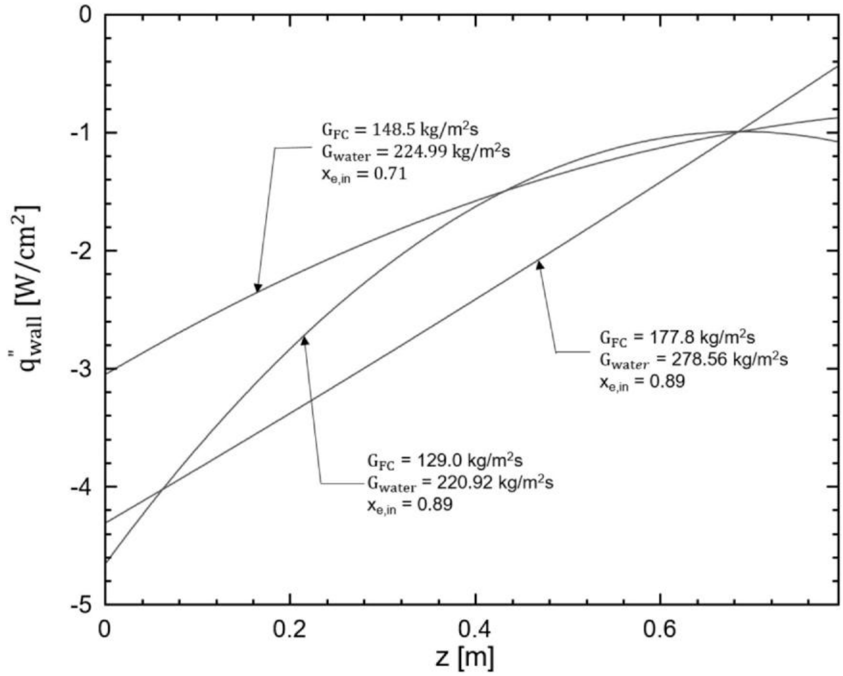

Fig. 5. Experimentally determined axial variations of wall heat flux for Test Cases 1,2 and 3 (Adapted from [40]).

$$S_g = -S_f = r_i \alpha_g \rho_g \frac{(T - T_{sat})}{T} \text{when condensing } (T < T_{sat}) \tag{5a}$$

and

$$S_g = -S_f = r_i \alpha_f \rho_f \frac{(T - T_{sat})}{T} \text{when evaporating } (T > T_{sat}) \tag{5b}$$

where r_i is the mass transfer intensity factor.

The second one derived from the Hertz–Knudsen equation [45]. The mass flux, $\dot{m}''$, is calculated based on the difference between the fluxes across the interface and given as

$$\dot{m}'' = \frac{2}{2-\gamma_c}\sqrt{\frac{M}{2\pi R}}\left[\gamma_c \frac{P_g}{\sqrt{T_g}} - \gamma_e \frac{P_f}{\sqrt{T_f}}\right] \tag{6}$$

where R is the universal gas constant, and γ_c and γ_e are molecules fractions condensing and evaporation, respectively. Researchers often set $\gamma_c = \gamma_e = \gamma$, where γ is the accommodation coefficient. A simplified model was developed by Tanasawa [46]. In this model, the interface temperature is set to saturation value. Also, the linear temperature change between the vapor and interface is used to estimate the heat flux. The corresponding mass flux is given as

$$\dot{m}'' = \frac{2\gamma}{2-\gamma}\sqrt{\frac{M}{2\pi R}}\frac{\rho_g h_{fg}(T - T_{sat})}{T_{sat}^{3/2}} \tag{7}$$

The corresponding source term can be determined by the following equation:

$$S_g = -S_f = \dot{m}'' \, |\nabla \alpha_g| \tag{8}$$

In this study, we will investigate the utilization of both the mass transfer models for flow condensation. For the Lee model [44], volumetric source is estimated by Eqs. (5a) and (5b), and for the Tanasawa [46] model, volumetric source is estimated by Eq. (8). The corresponding energy source Q due to phase-change in both cases is given by Eq. (4).

3.3. Computational domain

Fig. 3(a) shows the three-dimensional (3D) geometry for FC-72 flow inside the inner tube of CM-HT, and Fig. 3(b) shows the details of the two-dimensional (2D) axisymmetric computational domain used to simulate the condensation for this geometry. There is no gravitational acceleration component because of microgravity conditions onboard the parabolic flight; therefore, the axisymmetric domain is valid for any orientation. The computational domain has a width of half the hydraulic diameter of the circular tube, $W = D_h/2 = 3.56\ mm$. The condensation length of the computational domain under investigation is $L = 791.72\ mm$, the same as the length of the CM-HT module [40]. However, to avoid end effects caused by the outlet boundary of the domain, the total length of the domain is extended by around 1 m.

All mesh cells are quadrilateral in the computational domain. In most parts of the domain, the mesh size is kept uniform. However, the mesh is gradually refined when approaching the cooling wall, as shown in Fig. 3(b). This feature helps accurately capture thin liquid film formation, local turbulence, and strong gradients of temperature in this region.

3.4. Initialization and boundary conditions

Based on Table 1, the FC-72 thermodynamic equilibrium quality entering the test section was $x_{e,\ in} < 1$, which means that the FC-72 is in a saturated mixture state here. First, we verify the flow regime in the inlet domain for the three test cases. Based on the inlet conditions shown in Table 1, utilizing the flow regime maps presented in [49] for flow condensation, all three test cases are either wavy-annular or smooth-annular. With this known, for the inlet boundary condition, it is a not trivial task to specify the inlet velocity of each phase since we do not have a direct measure of the inlet void fraction, $\alpha_{g,\ in}$, The inlet void fraction, $\alpha_{g,\ in}$, is defined as the fraction of the cross-sectional area occupied by the vapor phase given by

$$\alpha_{g,in} = \frac{A_{g,in}}{A} = \frac{\pi(R - \delta_i)^2}{\pi R^2} \tag{9}$$

where δ_i is the liquid film initial thickness. The corresponding phase velocities are given by

$$u_{g,in} = \frac{W_{g,in}}{\rho_g A_{g,in}} = \frac{x_{in} W}{\alpha_{g,in}\rho_g A} \tag{10a}$$

and

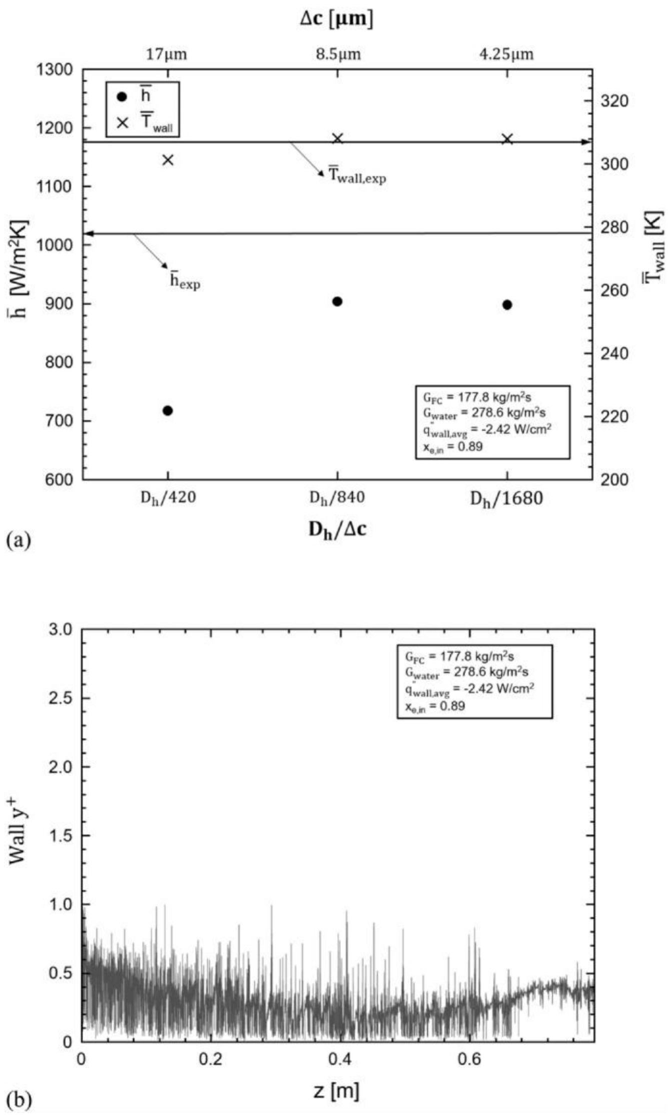

Fig. 6. (a) Average heat transfer coefficient and wall temperature variation for different mesh sizes for the test Case 3 from Table 1. (b) Wall y^+ along the condensation length for test Case 3 from Table 1.

$$u_{f,in} = \frac{W_{f,in}}{\rho_f A_{f,in}} = \frac{(1 - x_{in})W}{(1 - \alpha_{g,in})\rho_f A} \tag{10b}$$

where x_{in} is the inlet flow quality, which is equal to inlet thermodynamic equilibrium quality $x_{e,\ in}$ in the two-phase mixture region. Inlet flow quality, x_{in}, is a parameter that was measured experimentally by Lee et al. [40]. The relationship between x_{in} and $\alpha_{g,\ in}$is given by

$$\alpha_{g,in} = \left[1 + \frac{\rho_g u_{g,in}}{\rho_f u_{f,in}}\left(\frac{1 - x_{in}}{x_{in}}\right)\right]^{-1} \tag{11}$$

As shown in Eq. (11), volume fraction and velocity of each of the phases are coupled. Appropriate initial film thickness δ_i is needed to help determine the volume fraction. This initial thickness also helps reduces the convergence time for the simulation as will be discussed later. In this study, the control-volume based annular flow condensation model developed by Kim and Mudawar [47] is adapted to predict the initial thickness. Based on the model, conservation equations are solved upstream of the condensation section as shown in Fig. 4(a). The results are used to estimate the inlet vapor volume fraction and the corresponding initial film thickness. Table 2 shows the final equations, and Fig. 4(b) shows a flow chart with the solution procedure used to iteratively solve for the initial film thickness. The complete details of the procedure can be found in [47]. Finally, this computed initial film thickness will be used in Eqs. (9), (10a), (10b) to solve for the individual phase velocities at the inlet boundary. To mimic the annular flow boundary condition, we will have a central vapor core and outer liquid film region at the inlet boundary. The wavy annular flow regime will include inherent waviness, but for this simulation, it was not included because of the lack of available information on the transients. Fig. 3(b) shows how the inlet phase velocities, $u_{g,\ in}$ and $u_{f,\ in}$, are applied as boundary conditions to the computational domain. At the inlet boundary, in addition to the velocity conditions, the turbulence intensity, I_k, is calculated individually for both the phases given by [48],

$$I_k = \frac{u_k{'}}{u_k} = 0.16 Re_{D_h,k}^{-1/8} \tag{18}$$

where k is either phase g or phase f.

A challenge that we faced during setting up these simulations was the difficulty in generating a continuous film. It was observed that in the inlet region, the film would easily rupture and the entrained droplets would escape to the vapor core instead of forming a continuous liquid film. Increasing the mass transfer intensity factor, r_i, or the accommodation coefficient, γ, is supposed to help solve this problem. However, a large value of these constants can cause numerical convergence problems as discussed by [27]. Therefore, this study adopts another approach to assist in generation of the liquid film in the inlet domain. A thin initial thickness, δ_i, derived from the annular model [47] is applied to the inlet condensation length up to z = 0.20 m. Based on the model, the thickness for the three test cases under investigation varies between 68~142 μm, which is less than 2% of the tube diameter. This is a reasonable assumption because the predicted downstream film thickness is much thicker than the initial thickness computed by the annular model, and the converged simulation film thicknesses exceed this initial thickness.

The wall heat flux profile (Fig. 5) was made available from the PU-BTPFL experimental database. A UDF is used to set the heat flux boundary condition on the outer wall based on experimental data. Since the condensation heat transfer is not sensitive to roughness height, roughness constant, and contact angle, these parameters are set to their default values, 0 m, 0.5 and 90°, respectively [33].

3.5. Grid convergence study and time step

Fig. 6(a) shows the averaged heat transfer coefficient and wall temperature over the condensation section, for the highest flow rate test case, Test Case 3, shown in Table 1. Both parameters reach asymptotic values when the mesh size $\Delta c < 17\mu m$. Therefore, the minimum mesh size used in the remainder of this study near the wall is $\Delta c = 4.25\mu m$. Fig. 6(b) shows the wall y^+ value along the channel for the test case. A value lower than 1 is required for capturing the turbulence close to the wall with the standard $k - \omega$ turbulence model. The y^+ is less than 1 over the whole computational domain as shown in the figure. In this study, the values of wall y^+ shown in this figure represent what was obtained for all the test cases under investigation.

The Global Courant number is set to be 2, the minimum time step size used is 10^{-7} s, the minimum step change factor is 0.5, and the maximum step change factor is 5. Based on these conditions, the corresponding time steps were variable in this study, with the time step varying with the velocity field.

4. Results and discussion

4.1. Lee model and Tanasawa model comparison

First, we want to verify the validity of the phase-change models for the tests under investigation in this study. For the Lee model [44], in two separate studies involving flow condensation, Lee et al. [33] and

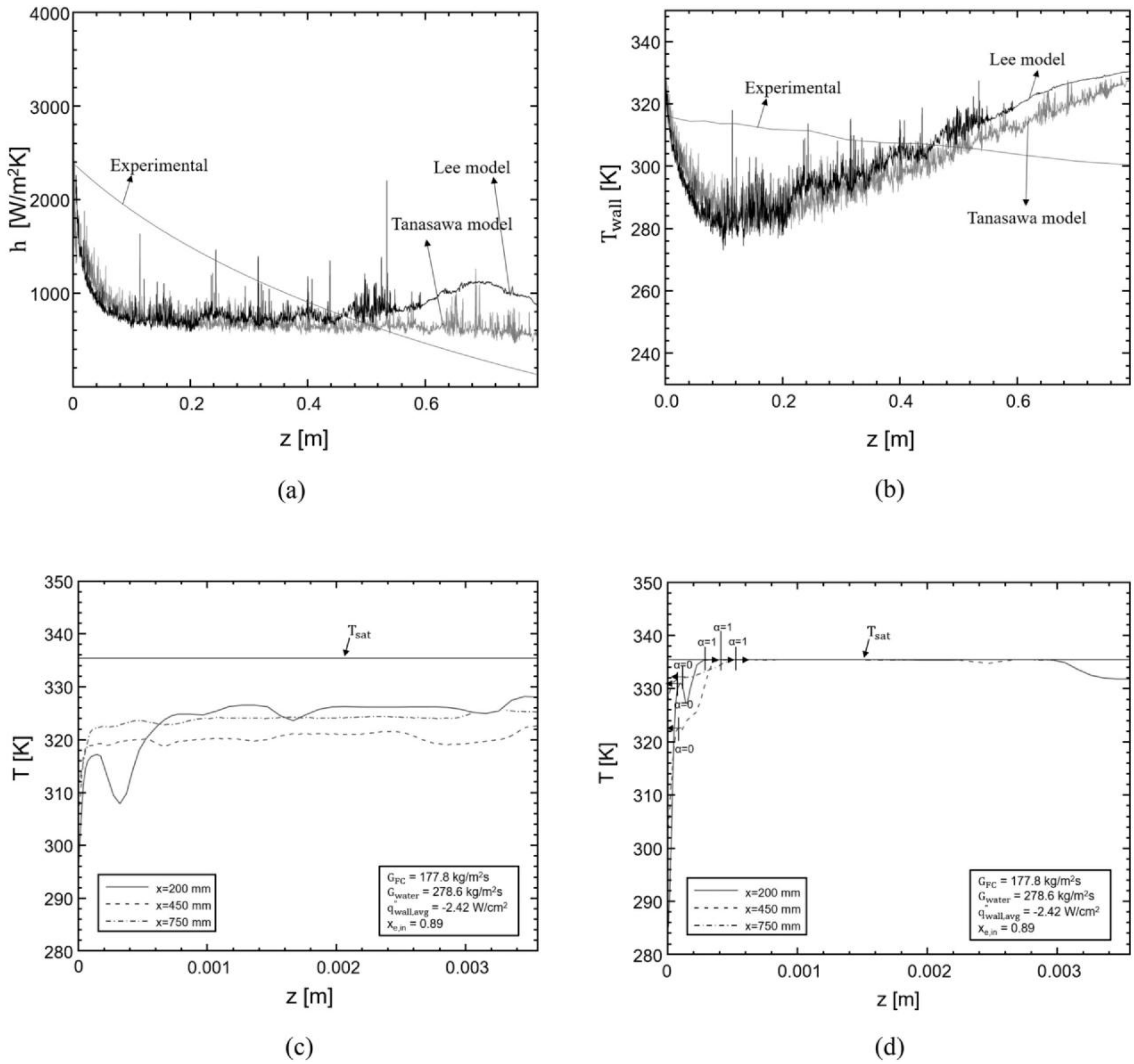

Fig. 7. Comparison between Tanasawa model and Lee model of (a) computed local condensation heat transfer coefficients and (b) computed local condensation wall temperature for test case 3. Computed fluid temperature versus distance from the wall at three axial locations derived by (c) Tanasawa model and (d) Lee model.

Table 3
Comparison of mass transfer rate predictions by Lee model and Tanasawa model for Test Case 3.

Mass transfer model	Equation	Equation parameters	[A]*	
Lee [44]	$S_g = -S_f = r_i \alpha_g \rho_g \frac{T - T_{sat}}{T_{sat}}$	$[A] = r_i$; $[B] = \rho_g \frac{T - T_{sat}}{T_{sat}}$; $[C] = \alpha_g$	10,000	
Tanasawa [46]	$S_g = -S_f = \dot{m}'' \ \lvert\nabla\alpha_g\rvert = \frac{2\gamma}{2-\gamma}\sqrt{\frac{M}{2\pi R}}\frac{\rho_g h_{fg}(T - T_{sat})}{T_{sat}^{3/2}} \ \lvert\nabla\alpha_g\rvert$	$[A] = \frac{2\gamma}{2-\gamma}\sqrt{\frac{M}{2\pi R T_{sat}}} h_{fg}$; $[B] = \rho_g \frac{T - T_{sat}}{T_{sat}}$; $[C] = \lvert\nabla\alpha_g\rvert$	γ	[A]
			1	773.50
			0.01	3.89
			1×10^{-4}	0.04

* For Test Case 3: $R = 8.314 \ J/mol \cdot K$, $M = 338 g/mol$, $h_{fg} = 8.8 \times 10^4 J/kg$.

Kharangate et al. [34] tested different values of $r_i$and concluded that $r_i = 10{,}000$ is appropriate to predict the mass transfer rate for both gravity assisted and gravity opposing flows in vertical orientations. For the Tanasawa model [46], in our study, an accommodation coefficient, γ, of 10^{-4} was selected. While different values of γ were tested in the simulation between 0 and 1, it was observed that lower values of γ increases deviation from saturation temperatures and higher values make the numerical model very unstable. A value higher than 10^{-4} is desirable, but it was observed that it would cause the CFD simulation to diverge. Fig. 7(a) and (b) show the comparison of the experimental and predicted heat transfer coefficient and wall temperatures when utilizing the Lee model and the Tanasawa model, respectively. The variations of

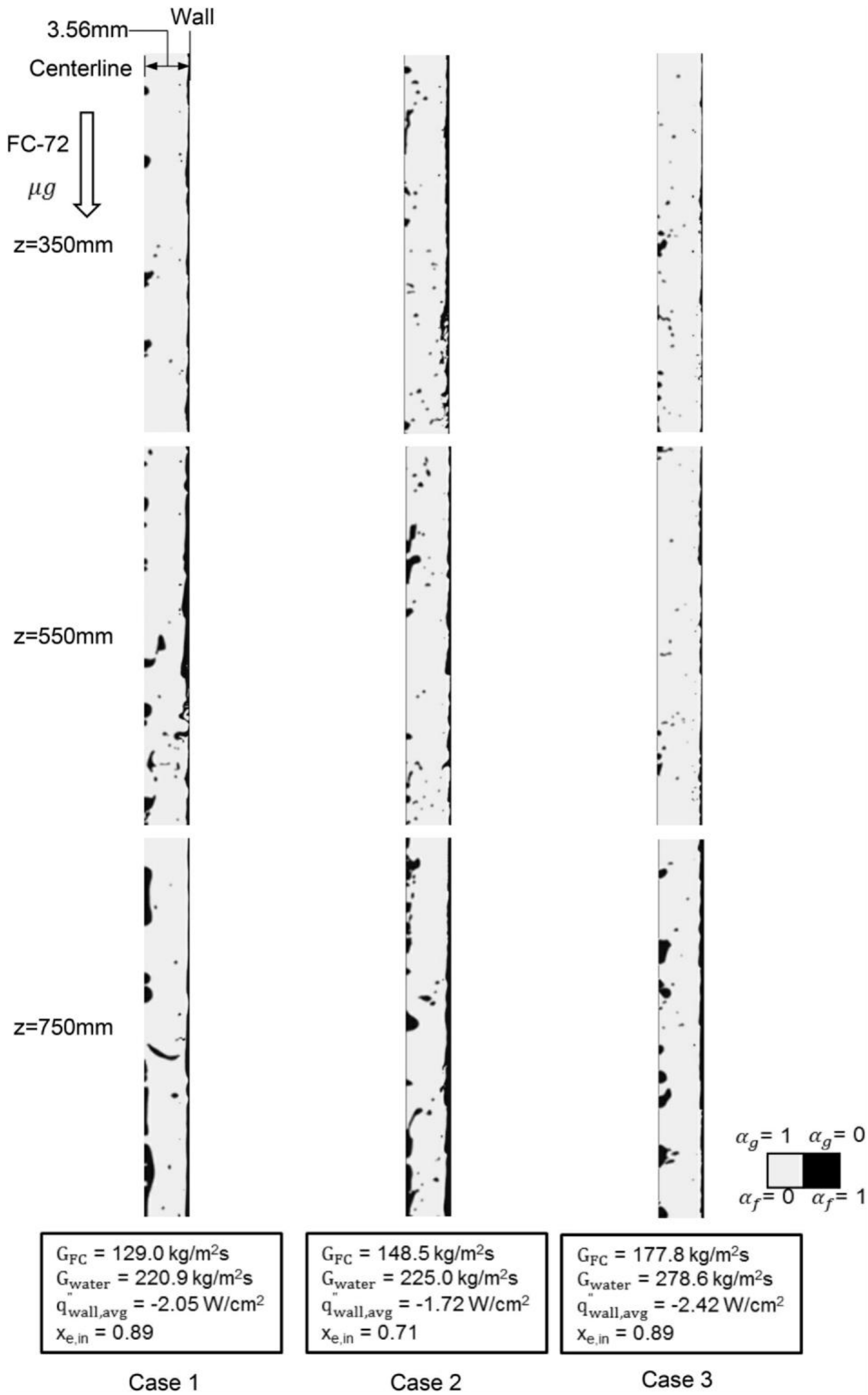

Fig. 8. Computed instantaneous volume fraction contour plots for the 3 test cases, centered at 3 axial locations along the condensation channel.

both the model results have similar trends. There is no significant difference to show if any model outperforms the other model in capturing the local variations in heat transfer or wall temperatures. Now let us look at the temperature profiles at three locations along the domain axis as shown in Fig. 7(c) and (d). For the Tanasawa model in Fig. 7(c), we notice that the temperature of the vapor core is significantly below the saturation value. Physically, condensation should happen while maintaining the vapor phase and the interface at the saturation condition. This indicates that for the present study, the Tanasawa model cannot correctly simulate the rate of phase-change. This underprediction in temperature is because γ is too small for this test case, and the mass source term does not match the actual mass transfer rate required to balance the temperature and energy across the interface. On the other hand, for the Lee model in Fig. 7(d), we see saturation conditions in the vapor core with large temperature gradients at the cooling wall and around the two-phase interface, that validate the mass transfer rate for the test conditions under investigation. To understand the difference between the two models, we try to do a one-to-one comparison of the constants in the Eqs. (5a) and (8) as shown in Table 3. The differences in the two equations are the parameters [A] and [C]. [C] is based on the

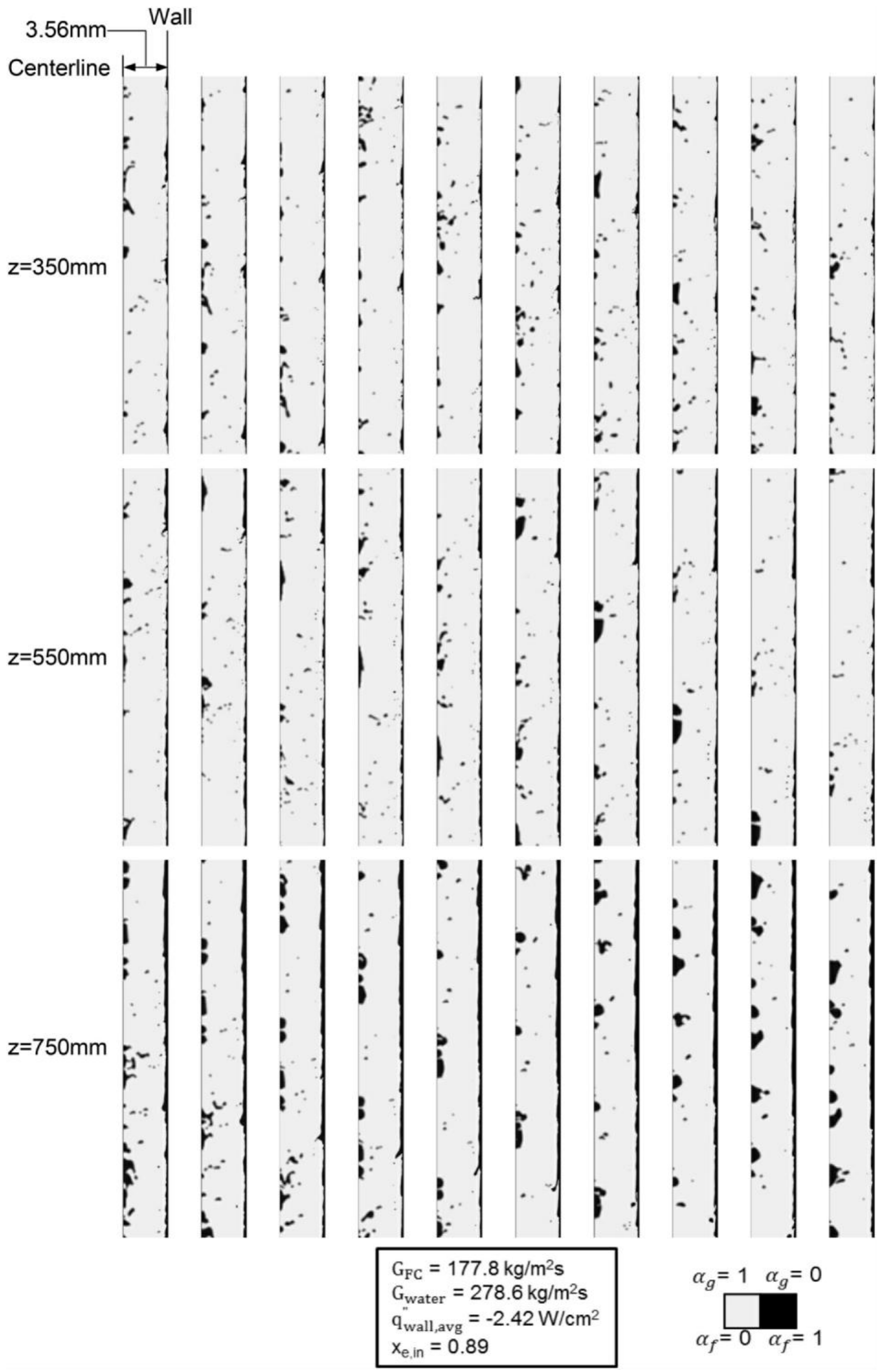

Fig. 9. Sequential time evolution of volume fraction contours for Test Case 3 with individual images 0.003 s apart.

void fraction or the gradient of void fraction. However, we observe that in the constant [A], there is a difference of at least one order of magnitude in the volumetric mass source rates predicted by the Tanasawa model in comparison to the Lee model, even in case of full condensation, i.e. when utilizing an accommodation coefficient $\gamma = 1$. Even if we solve the numerical convergence problems with the higher accommodation coefficients, the highest value for constant [A] will be 773, and the study by Lee et al. [33] showed that $r_i = 1000$ or lower is not able to capture the saturations conditions in the vapor core accurately. Hence, the Tanasawa model is not valid for the flow condensation scenario under investigation in this study. Therefore, going forward, only the results based on the Lee model will be discussed in this study.

4.2. Volume fraction results

Fig. 8 shows computed volume fraction contour plots of the 3 test cases investigated in this study with mass flow rates of G_{FC}=129.0, 148.5, 177.8 kg/m^2s. Instantaneous volume fraction contour plots are shown in this figure for each of these test cases, at three locations, representing the inlet, middle and exit sections in the tube centered at z= 350 mm, 550 mm, and 750 mm, respectively, with each section being 30 mm in length. The images show how the liquid film entering at

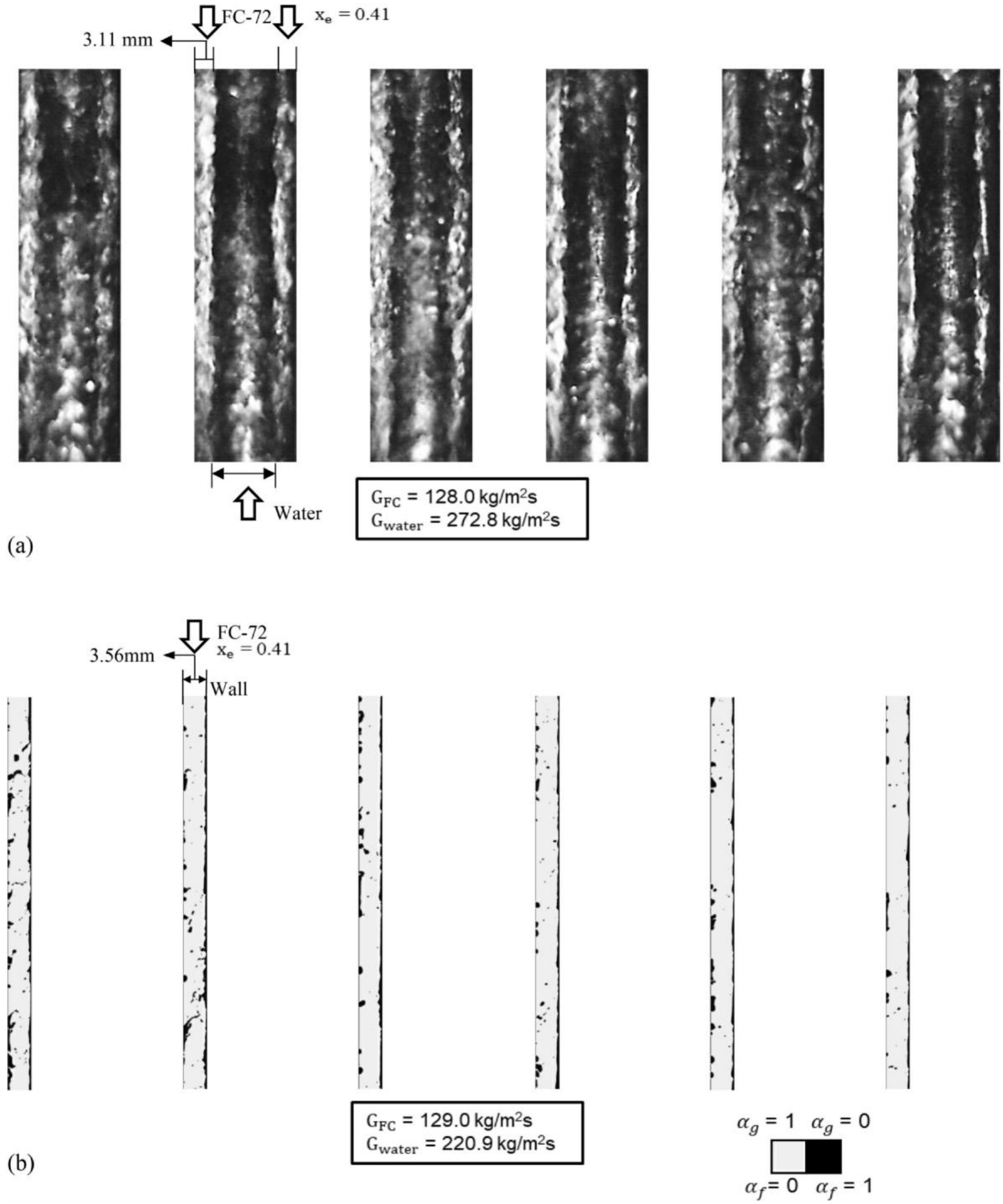

Fig. 10. (a) Time sequential images of liquid film from flow visualization module CM-FV with individual images 0.03 s apart (Adapted from [40]). (b) Time sequential images of computed volume fraction contour with individual images 0.03 s apart.

the inlet domain sees strong interfacial waves inherent to annular film condensation. In general, the liquid film is expected to become thicker in the flow direction, and this is a direct result of the condensation occurring in that direction. For the higher mass velocities, the liquid film did show a gradual increase along the flow domain. However, it was observed that for the lowest mass velocity test cases, the film thickness in the exit region is less than that in the inlet region. This is caused by the liquid accumulation in the vapor core region. Liquid entrainment and deposition observed in the flow are expected flow behaviors. However, liquid accumulations in the core is a result of the 2D axisymmetric domain not allowing liquid droplets to cross over to the opposite wall. The reason for this will be detailed later.

Fig. 9 shows the sequential images of the volume fraction contour plots for Test Case 3. The time interval between two consecutive images is 0.003 s, and each segment is centered around the same axial location, shown previously in Fig. 8. The complex motion of the liquid film can be observed in these time sequence plots. We observe that the liquid generated near the cooling wall has a tendency to move towards the centerline of the domain. Interfacial waviness, which can be observed at the liquid-vapor interface, causes some small liquid mass to detach from the liquid film. These liquid drops move towards the centerline. Kharangate et al. [34] explained that this behavior is caused by the entrained liquid having an radial velocity towards the center of the domain after breakup from the liquid film. We see that if the liquid droplets move towards the center, they cannot travel across the centerline due to the axis boundary condition, resulting in some liquid

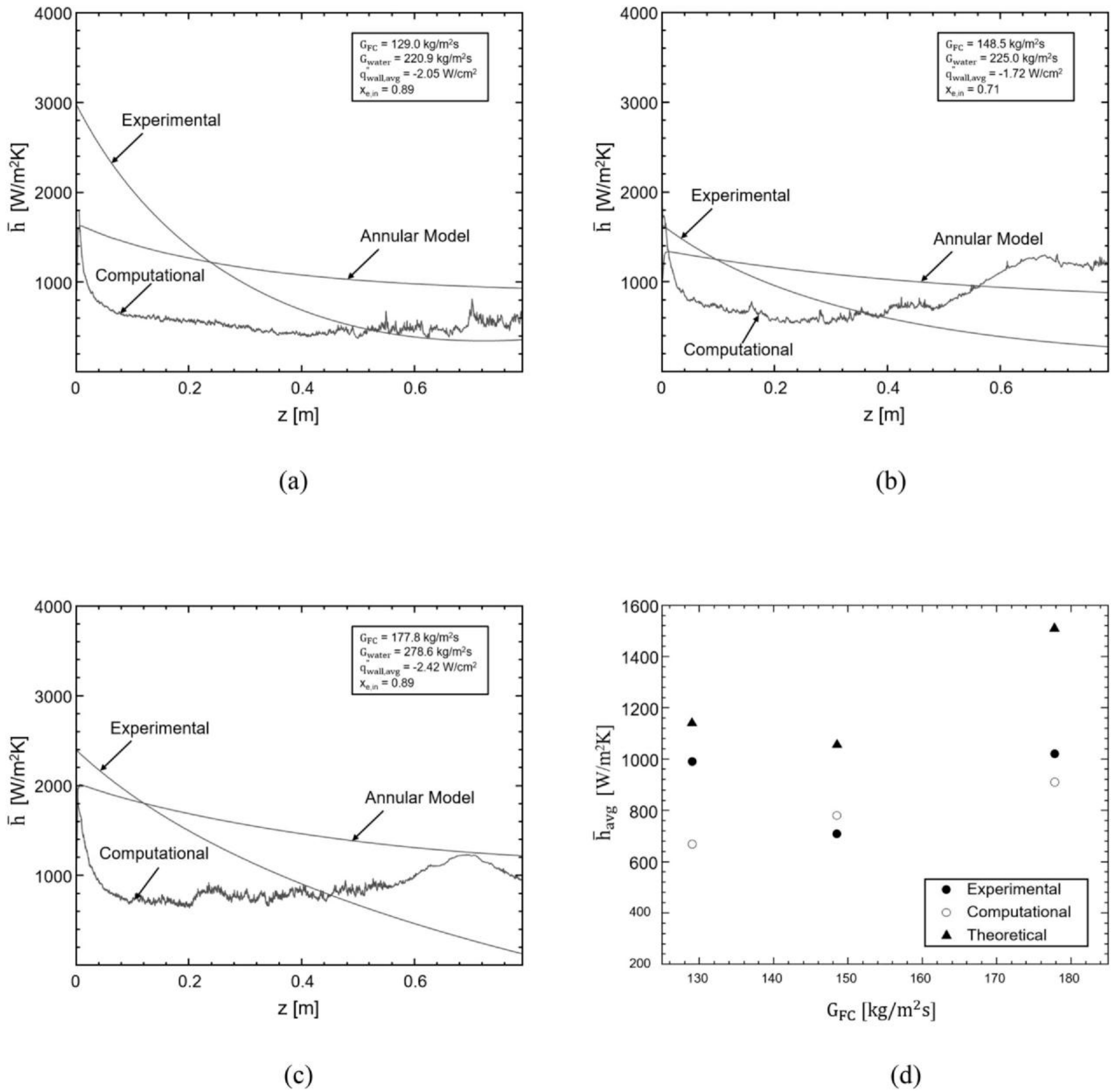

Fig. 11. Comparison of experimental [40], theoretical and computed local condensation heat transfer coefficients for (a) Test Case 1, (b) Test Case 2, and (c) Test Case 3. (d) Comparison of experimental, theoretical, and computed averaged condensation heat transfer coefficients with mass velocity.

accumulation. Numerically, this shortcoming is a direct consequence of the nature of our computational domain. In a full 3D domain, the condensing flow will not be exactly axisymmetric, and the entrained droplets will be able to cross over to the opposite side of the circular wall or be entrained as small liquid drops without accumulating at the centerline.

Fig. 10(a) shows sequential images of condensation in the flow visualization test section CM-FV data obtained from [40]. Each image is 4 cm in length and centered at $z = 580mm$ for similar FC-72 flow rate and mean thermodynamic equilibrium quality as the computational Test Case 1 in Table 1. Fig. 10(b) shows computed images of Test Case 1 at the same axial location and length, based on the heat transfer module, CM-HT. The time interval between two consecutive images in both figures is 0.03 s. The flow visualization images show that the flow is highly turbulent with the existence of interfacial features like small ripples and large waves. Because of the lower quality of these flow visualization images in Fig. 10(a), we cannot get a direct comparison of the flow behavior. However, both experimental and computational simulations show liquid film movement along the channel with strong interfacial waviness and entrained liquid drops in the vapor region.

4.3. Heat transfer coefficient results

Complex interfacial behavior, such as interfacial waviness, causes the film thickness to continuously change along the wall, which results in fluctuating wall temperatures and corresponding heat transfer coefficients. In order to account for these fluctuations and not capture local transient trends, simple time averaging is performed. The time-period of averaging is given by

$$\Delta t = L/u_{g,in} \tag{19}$$

where L is the total test section length and $u_{g,\ in}$ is the velocity of the vapor phase. The time-averaged local heat transfer coefficient is calculated by

$$\bar{h} = \frac{1}{\Delta t}\int_0^{\Delta t} h(z,t)dt \tag{20}$$

Fig. 11(a)–(c) shows a comparison of heat transfer coefficient

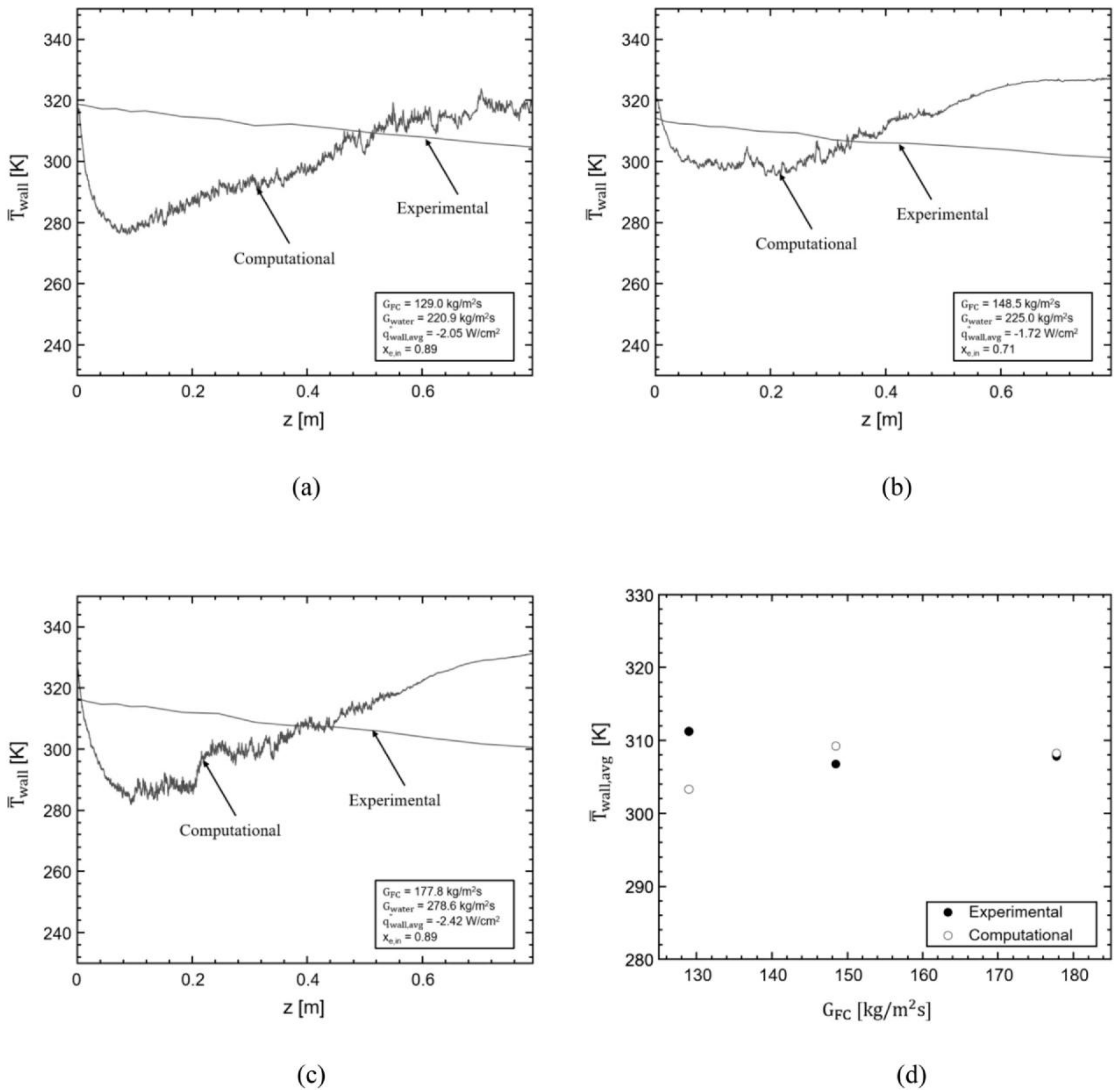

Fig. 12. Comparison of experimental [40], theoretical, and computed local wall temperature for (a) Test Case 1, (b) Test Case 2, and (c) Test Case 3. (d) Comparison of experimental and computed averaged wall temperature with mass velocity.

between the computed data, experimental data from PU-BTPFL database, and theoretical predicted data computed with the condensation model by Park et al. [48], for mass velocities of $G_{FC}=129.0$, 148.5, and 177.8 kg/m^2s, respectively. Both experimental and computed heat transfer coefficient show a larger value in the inlet region, where the film is thin and starting to form. In this region, the local heat transfer coefficient is under-predicted computationally. In the middle region, for all three mass velocities the experimental data and the computational results agree well. A reason for this is that the computational model does not predict the film thickness growth in the upstream region, where film initialization was utilized to aid liquid film formation as discussed earlier. However, as the film formation stabilizes and becomes thicker in the middle region, the predictions improve. The 2-D axisymmetric computational domain causes liquid droplet accumulation at the centerline in the exit region, as was observed in the void fraction plots shown in Figs. 8 and 9. This prevents the liquid droplet redeposit to the film, resulting in smaller film thickness in this region. This causes the computed local heat transfer coefficient to be over-predicted in this downstream region because of a thinner liquid film. The computed spatially averaged local heat transfer coefficient agrees well with the data as shown in Fig. 11(d). The higher variation in the lowest mass velocity test case is caused by the significantly higher liquid accumulation in the vapor core.

The flow condensation model by Park et al. [48] is a control-volume-based theoretical model that has shown good predicting performance for a similar diameter tube-in-tube condensation configuration for both local and average heat transfer data. Therefore, we select this model in our study for comparison with the computational and experimental results. We can see in Fig. 11(a)–(c) that the flow condensation model results follow the same trend as the experimental data. However, the local variations are not captured that well across the whole length of the computational domain by the model. The computational model captures the local behavior better in comparison to the annular flow model. Even though the predictions of liquid entrainment and deposition in the computed results have shortcomings like unnecessary accumulation in the vapor core, the annular flow model does now have the ability to account for any of this, and therefore, is less accurate.

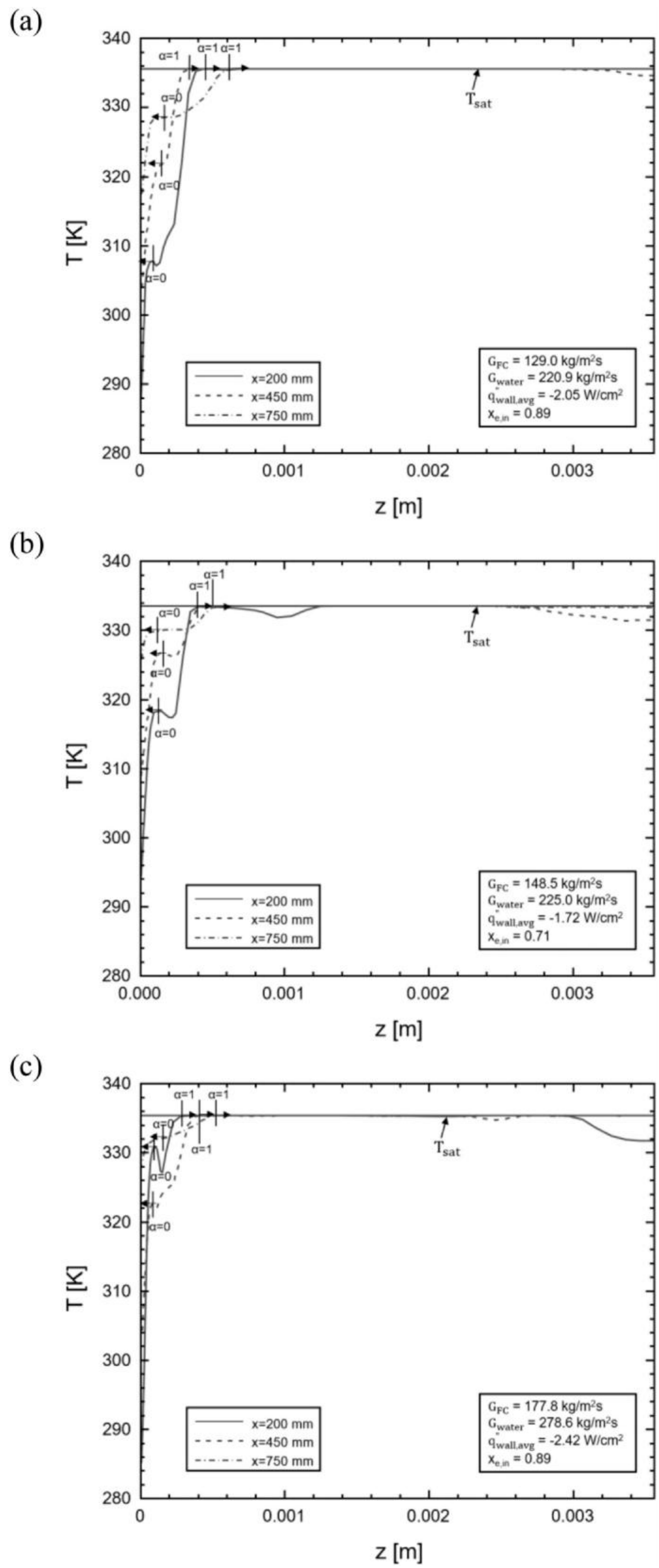

Fig. 13. Computed fluid temperature versus distance from the wall at three axial locations for (a) Test Case 1, (b) Test Case 2, and (c) Test Case 3.

4.4. Temperature results

Fig. 12(a)–(c) shows the comparison between the computed local wall temperature variations, time-averaged over period Δt, in the axial direction and the experimental data, for mass velocities of $G_{FC} = 129.0$, 148.5, 177.8 kg/m^2s. The experimental data of wall temperature shows an almost linear decline with the condensation length. However, computed wall temperature decreases in the upstream region, then increases with condensation length in the downstream region. Notice that, the trend of variation in predicted local wall temperature is similar to the trend of local heat transfer coefficient, as discussed earlier. Because the experimentally measured wall heat flux is used in the computational simulation as a BC, the under-prediction or improvement in heat transfer is a direct consequence of wall temperature. Fig. 12(d) compares the computed spatially averaged wall temperature with experimental data for the three mass velocities. All of the three test cases show the computational and experimental results of wall temperature agree reasonably well. The predicting capability of the computational simulation is seen to be better for higher mass velocities.

Fig. 13(a)–(c) shows the temperature profile across the vapor core and liquid film in the radial direction, at three axial locations, $z = 200$, 450, 700 mm, respectively, along the channel. These images show that the temperature across the two-phase interface and the vapor region is reasonably close to the saturation condition of the fluid. This is an important check for confirming the validity of the two-phase condensation simulation. If the saturation temperatures are not maintained in those regions, the mass transfer rates are not sufficient and need adjustment. In the volume fraction plots shown in Figs. 8 and 9, the liquid entrainment effect is seen to causes some liquid droplet accumulation at the centerline of the channel. This explains the temperature drops near the centerline, where we observe temperatures lower than the saturation temperature. The temperature profile shows a large slope in the interfacial region and the wall, but a mild slope in the center of the liquid region. This feature of a large temperature change at the interface was also captured in earlier studies on vertical upflow condensation [34] and vertical downflow condensation [33], and is related to the damping of turbulent fluctuations in the liquid-vapor interfacial region.

5. Need for *3D CFD*

The present study utilized a 2D axisymmetric domain to investigate annular flow condensation in a circular tube with two-phase inlet conditions under microgravity. While some promising results are obtained in terms of the capturing the two-phase interfacial behavior, the averaged heat transfer coefficient data and the averaged wall temperature data, the results point to a need for further improvement in the CFD model to be able to better predict liquid entrainment and liquid deposition phenomena observed within the condensing flow. The simulation results show that liquid accumulation in the vapor core region impacts predictions of heat transfer coefficients and wall temperatures. Going forward, there is a need to move to a full 3D computational domain. Some prior computational studies, discussed in the introduction, have performed 3D investigations involving micro/mini-channel flow condensation [27,31,32], but there is a limited effort made in investigating a full-scale highly turbulent condensation problem in macro-sized channels in 3D. Our large computation domain size and highly turbulent two-phase inlet flow conditions present these as the main challenges in developing a full 3D model. Any future work will need to address them satisfactorily to improve the predicting capability of the computational models.

6. Conclusions

This study investigated annular flow condensation of FC-72 in microgravity with two-phase inlet conditions, computationally, utilizing the VOF multi-phase model. The phase-change at the two-phase interface was simulated utilizing the Lee model [44] and also compared with the Tanasawa model [46]. The CFD model predictions were compared with available data from the PU-BTPFL database. The important conclusions are as follows.

(1) The model incorporated with the Tanasawa mass transfer model suffered from numerical stability issues and was shown to be invalid for the current flow condensation configuration.
(2) The computational model incorporated with the Lee mass transfer model predicts complex two-phase interfacial behavior observed in condensing flows. However, the domain suffered from some issues of liquid accumulation in the vapor core.
(3) Local heat transfer coefficient and wall temperature are under-predicted in the inlet region of the channel, and over-predicted in the outlet region of the channel, compared with the experimental measurements.
(4) The computed temperature profile of the cross-section showed that the temperature was maintained close to saturation temperatures across the interface and in the vapor, showing that the Lee mass transfer model was able to simulate the condensation accurately.
(5) Results show a need for full 3D simulations of flow condensation to improve predictions of liquid entrainment and liquid deposition phenomena that significantly impact local heat transfer coefficients predictions.

Declaration of Competing Interest

The authors declare that they have no known competing financial interests or personal relationships that could have appeared to influence the work reported in this paper.

Acknowledgment

The authors thank Purdue University Boiling and Two-Phase Flow Laboratory (PU-BTPFL) for sharing experimental data that was used for validation of the computational model developed in this study. This work made use of the High Performance Computing Resource in the Core Facility for Advanced Research Computing at Case Western Reserve University.

References

[1] I. Mudawar, Assessment of high-heat-flux thermal management schemes, IEEE Trans. Components Packag. Technol. 24 (2001) 122–141, https://doi.org/10.1109/6144.926375.
[2] W. Qu, I. Mudawar, Flow boiling heat transfer in two-phase micro-channel heat sinks—I. experimental investigation and assessment of correlation methods, Int. J. Heat Mass Transf. 46 (2003) 2755–2771, https://doi.org/10.1016/S0017-9310(03)00041-3.
[3] H.J. Lee, S.Y. Lee, Heat transfer correlation for boiling flows in small rectangular horizontal channels with low aspect ratios, Int. J. Multiph. Flow. 27 (2001) 2043–2062.
[4] M. Monde, T. Inoue, Critical heat flux in saturated forced convective boiling on a heated disk with multiple impinging jets, J. Heat Transf. 113 (1991) 722–727.
[5] D.C. Wadsworth, I. Mudawar, Enhancement of single-phase heat transfer and critical heat flux from an ultra-high-flux simulated microelectronic heat source to a rectangular impinging jet of dielectric liquid, J. Heat Transf. 114 (1992) (Transactions ASME (American Soc. Mech. Eng. Ser. C);(United States).
[6] L. Lin, R. Ponnappan, Heat transfer characteristics of spray cooling in a closed loop, Int. J. Heat Mass Transf 46 (2003) 3737–3746.
[7] J.G. Collier, J.R. Thome, Convective Boiling and Condensation, Clarendon Press, 1994.
[8] D.P. Traviss, W.M. Rohsenow, Flow regimes in horizontal two-phase flow with condensation, ASHRAE Trans. 79 (1973) 31–39.
[9] Y. Taitel, A.E. Dukler, A model for predicting flow regime transitions in horizontal and near horizontal gas-liquid flow, AICHE J. 22 (1976) 47–55.
[10] J. El Hajal, J.R. Thome, A. Cavallini, Condensation in horizontal tubes, part 1: two-phase flow pattern map, Int. J. Heat Mass Transf. 46 (2003) 3349–3363.
[11] H.M. Soliman, On the annular-to-wavy flow pattern transition during condensation inside horizontal tubes, Can. J. Chem. Eng. 60 (1982) 475–481.
[12] L.P. Golan, A.H. Stenning, Two-Phase Vertical Flow Maps, in: Proc. Inst. Mech. Eng. Conf. Proc. SAGE Publications Sage UK, London, England, 1969, pp. 108–114.
[13] T. Oshinowo, M.E. Charles, Vertical two-phase flow part I. Flow pattern correlations, Can. J. Chem. Eng. 52 (1974) 25–35.
[14] X. Huang, G. Ding, H. Hu, Y. Zhu, H. Peng, Y. Gao, B. Deng, Influence of oil on flow condensation heat transfer of R410A inside 4.18 mm and 1.6 mm inner diameter horizontal smooth tubes, Int. J. Refrig. 33 (2010) 158–169.
[15] J.E. Park, F. Vakili-Farahani, L. Consolini, J.R. Thome, Experimental study on condensation heat transfer in vertical minichannels for new refrigerant R1234ze (E) versus R134a and R236fa, Exp. Thermal Fluid Sci. 35 (2011) 442–454.
[16] W.W. Akers, Condensation Inside Horizontal Tubes, in: Chem. Engg. Prog. Symp. Ser. (1960), p. 145.
[17] A. Cavallini, R. Zecchin, A Dimensionless Correlation for Heat Transfer in Forced Convection Condensation, in: Proc. Sixth Int. Heat Transf. Conf. (1974), pp. 309–313.
[18] M.M. Shah, A general correlation for heat transfer during film condensation inside pipes, Int. J. Heat Mass Transf. 22 (1979) 547–556, https://doi.org/10.1016/0017-9310(79)90058-9.
[19] M.M. Shah, An improved and extended general correlation for heat transfer during condensation in plain tubes, Hvac&R Res. 15 (2009) 889–913.
[20] H. Haraguchi, Condensation of refrigerants HCFC22, HFC134a and HCFC123 in a horizontal smooth tube, Trans. Japan Soc. Mech. Eng. 60 (1994) 245–252.
[21] M.K. Dobson, J.C. Chato, Condensation in smooth horizontal tubes, J. Heat Transf. 120 (1998) 193–213 https://doi.org/10.1115/1.2830043.
[22] S. Koyama, K. Kuwahara, K. Nakashita, K. Yamamoto, An experimental study on condensation of refrigerant R134a in a multi-port extruded tube, Int. J. Refrig. 26 (2003) 425–432.
[23] T. Bohdal, H. Charun, M. Sikora, Comparative investigations of the condensation of R134a and R404A refrigerants in pipe minichannels, Int. J. Heat Mass Transf. 54 (2011) 1963–1974.
[24] S.-M. Kim, I. Mudawar, Universal approach to predicting heat transfer coefficient for condensing mini/micro-channel flow, Int. J. Heat Mass Transf. 56 (2013) 238–250.
[25] S.-M. Kim, I. Mudawar, Universal approach to predicting two-phase frictional pressure drop for adiabatic and condensing mini/micro-channel flows, Int. J. Heat Mass Transf. 55 (2012) 3246–3261.
[26] S.M. Kim, I. Mudawar, Theoretical model for local heat transfer coefficient for annular flow boiling in circular mini/micro-channels, Int. J. Heat Mass Transf. 73 (2014) 731–742, https://doi.org/10.1016/j.ijheatmasstransfer.2014.02.055.
[27] E. Da Riva, D. Del Col, Effect of gravity during condensation of R134a in a circular minichannel, Microgravity Sci. Technol. 23 (2011) 87.
[28] H. Ganapathy, A. Shooshtari, K. Choo, S. Dessiatoun, M. Alshehhi, M. Ohadi, Volume of fluid-based numerical modeling of condensation heat transfer and fluid flow characteristics in microchannels, Int. J. Heat Mass Transf. 65 (2013) 62–72.
[29] L. Vyskocil, J. Schmid, J. Macek, CFD simulation of air–steam flow with condensation, Nucl. Eng. Des. 279 (2014) 147–157, https://doi.org/10.1016/J.NUCENGDES.2014.02.014.
[30] Z. Yin, Y. Guo, B. Sunden, Q. Wang, M. Zeng, Numerical simulation of laminar film condensation in a horizontal minitube with and without non-condensable gas by the VOF method, Numer. Heat Transf. Part A Appl. 68 (2015) 958–977.
[31] G.D. Qiu, W.H. Cai, Z.Y. Wu, Y. Yao, Y.Q. Jiang, Numerical simulation of forced convective condensation of propane in a spiral tube, J. Heat Transfer. 137 (2015), https://doi.org/10.1115/1.4029475.
[32] J. Zhang, W. Li, W.J. Minkowycz, Numerical simulation of condensation for R410A at varying saturation temperatures in mini/micro tubes, Numer. Heat Transf. Part A Appl. 69 (2016) 464–478.
[33] H. Lee, C.R. Kharangate, N. Mascarenhas, I. Park, I. Mudawar, Experimental and computational investigation of vertical downflow condensation, Int. J. Heat Mass Transf. 85 (2015) 865–879, https://doi.org/10.1016/j.ijheatmasstransfer.2015.02.037.
[34] C.R. Kharangate, H. Lee, I. Park, I. Mudawar, Experimental and computational investigation of vertical upflow condensation in a circular tube, Int. J. Heat Mass Transf. 95 (2016) 249–263, https://doi.org/10.1016/j.ijheatmasstransfer.2015.11.010.
[35] J. Zhang, W. Li, Numerical study on heat transfer and pressure drop characteristics of R410A condensation in horizontal circular mini/micro-tubes, Can. J. Chem. Eng. 94 (2016) 1809–1819, https://doi.org/10.1002/cjce.22554.
[36] J. Wen, X. Gu, S. Wang, Y. Li, J. Tu, Numerical investigation on condensation heat transfer and pressure drop characteristics of R134a in horizontal flattened tubes, Int. J. Refrig. 85 (2018) 441–461, https://doi.org/10.1016/J.IJREFRIG.2017.10.024.
[37] H. Deng, J. Liu, T. Yang, S. Wu, Numerical study and visualization on flow characteristics of reflux condensation in air-cooled condenser, Appl. Therm. Eng. 148 (2019) 1310–1323, https://doi.org/10.1016/J.APPLTHERMALENG.2018.11.109.
[38] Z. Zhao, Y. Zhang, X. Chen, X. Ma, S. Yang, S. Li, A numerical study on condensation flow and heat transfer of refrigerant in minichannels of printed circuit heat exchanger, Int. J. Refrig. 102 (2019) 96–111, https://doi.org/10.1016/J.IJREFRIG.2019.03.016.
[39] S.M.A.N.R. Abadi, W.A. Davies, P. Hrnjak, J.P. Meyer, Numerical study of steam condensation inside a long inclined flattened channel, Int. J. Heat Mass Transf. 134 (2019) 450–467, https://doi.org/10.1016/J.IJHEATMASSTRANSFER.2019.01.063.
[40] H. Lee, I. Mudawar, M.M. Hasan, Experimental and theoretical investigation of annular flow condensation in microgravity, Int. J. Heat Mass Transf. 61 (2013) 293–309, https://doi.org/10.1016/j.ijheatmasstransfer.2013.02.010.
[41] H. Lee, I. Mudawar, M.M. Hasan, Flow condensation in horizontal tubes, Int. J. Heat Mass Transf. 66 (2013) 31–45.
[42] A. Fluent, 12.1 in Workbench User's Guide, ANSYS Inc., Canonsburg, PA, 2009.
[43] J. Brackbill, D. Kothe, C. Zemach, A continuum method for modeling surface tension, J. Comput. Phys. 100 (1992) 335–354, https://doi.org/10.1016/0021-9991(92)90240-Y.
[44] W.H. Lee, Pressure Iteration Scheme for Two-Phase Flow Modeling, in Multiph. Transp. Fundam. React. Safety, Appl, (1980), pp. 407–432.
[45] R.W. Schrage, A Theoretical Study of Interphase Mass Transfer, Columbia University Press, 1953.

[46] I. Tanasawa, Advances in condensation heat transfer, Adv. Heat Transf. 21 (1991) 55–139.
[47] S.-M. Kim, I. Mudawar, Theoretical model for annular flow condensation in rectangular micro-channels, Int. J. Heat Mass Transf. 55 (2012) 958–970.
[48] I. Park, S.-M. Kim, I. Mudawar, Experimental measurement and modeling of downflow condensation in a circular tube, Int. J. Heat Mass Transf. 57 (2013) 567–581.
[49] I. Park, H. Lee, I. Mudawar, Determination of flow regimes and heat transfer coefficient for condensation in horizontal tubes, Int. J. Heat Mass Transf. 80 (2015) 698–716.
[50] G.B. Wallis, One-Dimensional Two-Phase Flow, McGraw-Hill, New York, 1969.